HHS Public Access

Author manuscript

Nat Chem. Author manuscript; available in PMC 2022 April 11.

Published in final edited form as:

Nat Chem. 2021 December ; 13(12): 1228–1234. doi:10.1038/s41557-021-00799-8.

Tracing the Incorporation of the "9th Sulfur" into the Nitrogenase Cofactor Precursor with Selenite and Tellurite

Kazuki Tanifuji[1,2], **Andrew J. Jasniewski**[1], **David Villarreal**[3], **Martin T. Stiebritz**[1], **Chi Chung Lee**[1], **Jarett Wilcoxen**[4], **Yasuhiro Okhi**[2], **Ruchira Chatterjee**[5], **Isabel Bogacz**[5], **Junko Yano**[5], **Jan Kern**[5], **Britt Hedman**[6], **Keith O. Hodgson**[6,7], **R. David Britt**[3,*], **Yilin Hu**[1,*], **Markus W. Ribbe**[1,8,*]

[1]Department of Molecular Biology and Biochemistry, University of California, Irvine, CA 92697-3900

[2]International Research Center for Elements Science, Institute for Chemical Research, Kyoto University, Uji, Kyoto 611-0011, Japan

[3]Department of Chemistry, University of California, Davis, CA 95616

[4]Department of Chemistry and Biochemistry, University of Wisconsin, Milwaukee, WI 53211

[5]Molecular Biophysics and Integrated Bioimaging Division, Lawrence Berkeley National Laboratory, Berkeley, CA 94720

[6]Stanford Synchrotron Radiation Lightsource, SLAC National Accelerator Laboratory, Stanford University, Menlo Park, CA 94025

[7]Department of Chemistry, Stanford University, Stanford, CA 94305

[8]Department of Chemistry, University of California, Irvine, CA 92697-2025

Abstract

The Mo-nitrogenase catalyzes the reduction of N_2 to NH_3 at its cofactor, an [(*R*-homocitrate)$MoFe_7S_9C$] cluster synthesized via the formation of a [Fe_8S_9C] L-cluster prior to the insertion of Mo and homocitrate. Previously, we have identified a [Fe_8S_8C] L*-cluster, which is homologous to the core structure of the L-cluster but lacks the '9th sulfur' in the belt region. However, direct evidence and mechanistic details of the L*- to L-cluster conversion upon '9th sulfur' insertion remain elusive. Here, we trace the '9th sulfur' insertion using SeO_3^{2-} and TeO_3^{2-} as 'labeled' SO_3^{2-}. Biochemical, EPR and XAS/EXAFS studies suggest a role of the '9th sulfur' in cluster transfer during cofactor biosynthesis while revealing the incorporation of Se^{2-}- and Te^{2-}-like species into the L-cluster. DFT calculations further point to a plausible mechanism

*Correspondence should be addressed to mribbe@uci.edu, yilinh@uci.edu and rdbritt@ucdavis.edu.

Author contributions

K.T., A.J.J., M.T.S., C.C.L, Y.H. and M.W.R. designed experiments. K.T., A.J.J., M.T.S., C.C.L, D.V., J.W., R.C., I.B., J.Y., J.K., R.D.B., Y.H. and M.W.R. analyzed data. K.T., A.J.J., M.T.S., C.C.L., D.V., J.W., R.C., I.B., J.Y and J.K. performed experiments. Y.O., B.H. and K.O.H provided material and/or technical resources. Y.H. and M.W.R. wrote the manuscript with input from all authors.

Competing interests

The authors declare no competing financial and non-financial interests.

involving *in-situ* reduction of SO_3^{2-} to S^{2-}, thereby suggesting the utility of this reaction to label the catalytically-important belt region for mechanistic investigations of nitrogenase.

Graphical Abstract

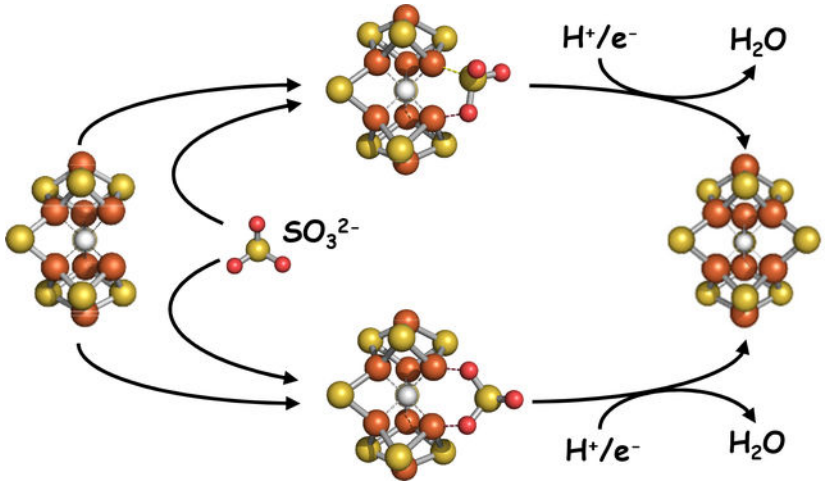

Introduction

Nitrogenase catalyzes the ambient reduction of dinitrogen to ammonia, a key step in the global nitrogen cycle, at its cofactor site.[1–4] Designated the M-cluster (or FeMoco), the cofactor of Mo-nitrogenase is a [(*R*-homocitrate)$MoFe_7S_9C$] cluster that can be viewed as [$MoFe_3S_3$] and [Fe_4S_3] subclusters bridged by three 'belt' μ_2-sulfides (S^{2-}) and one interstitial μ_6-carbide (C^{4-}); additionally, its Mo 'end' is ligated by an organic *R*-homocitrate moiety (Supplementary Fig. 1a).[5,6] Biosynthesis of the M-cluster (Supplementary Fig. 1a)[4,7–10] is initiated with the combined action of the cysteine desulfurase, NifS, and the scaffold protein, NifU, which enables the sequential formation of [Fe_2S_2] and [Fe_4S_4] clusters. Subsequently, a pair of [Fe_4S_4] clusters (designated the K-cluster) is transferred to NifB, an essential protein for cofactor biosynthesis, and converted to an [Fe_8S_9C] precursor (designated the L-cluster) concomitant with the insertion of an interstitial carbide in the center of the cluster and a '9^{th} sulfur' in its belt region.[6,11,12] The L-cluster is then transferred to NifEN, an indispensable assembly scaffold, where it is matured into a fully complemented M-cluster upon substitution of Mo/homocitrate for one of its terminal Fe atoms.[13,14] Once matured, the M-cluster is delivered from NifEN to its target binding site in NifDK, the catalytic component of Mo-nitrogenase, thereby completing the biosynthesis of this complex metallocofactor.[9,10]

Playing a pivotal role in nitrogenase cofactor biosynthesis, NifB catalyzes the most dramatic transformation of a pair of the 'usual' [Fe_4S_4] clusters into an [Fe_8S_9C] precursor with the 'unusual' geometry of the cofactor core. A member of the radical *S*-adenosyl-*L*-methionine (SAM) enzyme family, NifB contains a canonical CxxxCxxC motif for the ligation of a SAM-binding [Fe_4S_4] cluster (designated the SAM- or RS-cluster), as well as additional, conserved Cys and His ligands for the coordination of a [Fe_4S_4] cluster pair (*i.e.*, the K-cluster, with its two 4Fe modules designated the K1- and K2-

clusters, respectively).[15,16] Using a combination of biochemical, mutagenic, spectroscopic and structural approaches, we have confirmed the presence of SAM- and K-clusters on NifB and identified the respective ligands for these clusters through studies of NifB proteins from *Azotobacter vinelandii*, *Methanosarcina acetivorans* and *Methanobacterium thermoautotrophicum*.[5,11,12,16–18] More importantly, these studies have led us to the proposal of a radical SAM-dependent pathway of carbide insertion concomitant with the K- to L-cluster conversion on NifB (Supplementary Fig. 1b).[4,9,10] This pathway begins with transfer of a methyl group from one SAM molecule to the K2-cluster, followed by abstraction of a hydrogen atom from the K2-bound methyl group by a 5'-dA• radical that is derived from the homolytic cleavage of a second SAM molecule. The methyl-derived carbon radical then initiates radical-based coupling and rearrangement of K1- and K2-clusters while undergoing further deprotonation itself until a μ_6-coordinated carbide appears in the center of the cluster.

Importantly, the cluster rearrangement and carbide insertion on NifB are accompaned by the insertion of a '9th sulfur' in the belt region of the cluster, which completes the stoichiometry of the [Fe_8S_9C] L-cluster. Previously, by reconstituting the NifB protein from *M. acetivorans* (designated *Ma*NifB) with synthetic [Fe_4S_4] clusters, we generated a protein free of sulfur impurities introduced by the conventional $FeCl_3$/Na_2S reconstitution procedure for the subsequent studies of the origin and insertion of the '9th sulfur'.[11] These studies not only revealed sulfite (SO_3^{2-}) as a source of the '9th sulfur', but also identified a [Fe_8S_8C] precursor (designated the L*-cluster) that was formed upon incubation of *Ma*NifB-bound K-cluster with SAM in the absence of SO_3^{2-}.[11,12] Fe K-edge XAS/EXAFS and ESEEM analyses[12] pointed to a high degree of structural homology between the [Fe_8S_8C] L*-cluster and the [Fe_8S_9C] L-cluster, with the former closely resembling the latter in structure except for the absence of one belt μ_2-sulfide. This observation shed important light on the sequence of events between carbide and sulfur insertion during the cofactor assembly process, placing the insertion of the '9th sulfur' after the formation of an 8Fe cofactor core with the interstitial carbide already in place (*i.e.*, the L*-cluster). However, direct evidence for incorporation of SO_3^{2-} as the '9th sulfur' into the L*-cluster, as well as the mechanistic details of this reaction, remains elusive.

Results and Discussion

To trace the incorporation and transformation of SO_3^{2-}, we first examined whether heavy chalcogenide congeners, SeO_3^{2-} and TeO_3^{2-}, could substitute for SO_3^{2-} in the *in vitro* cofactor maturation assay. Consistent with the closely related reactivities of S, Se and Te, incubation of SO_3^{2-}, SeO_3^{2-} or TeO_3^{2-} with the SAM-treated *Ma*NifB in the presence of a sulfur-free reductant, Eu^{II}-EGTA, yielded *Ma*NifB species capable of donating the L-cluster (or its Se- or Te-substituted equivalent) that could be matured into an M-cluster (or its Se- or Te-substituted equivalent) on NifEN and subsequently used to reconstitute the cofactor-deficient apo NifDK (Fig. 1a; Supplementary Fig. 2a). In contrast, Se^{2-} or Te^{2-} was unable to support cluster maturation in the same *in vitro* assay (Supplementary Fig. 2a), consistent with our previous observation that S^{2-} was inactive in this reaction.[11] There was a difference in the concentration dependence of cofactor maturation activity with SO_3^{2-}, SeO_3^{2-} or TeO_3^{2-} as the source of the '9th sulfur'; most notably, the activity reached

the maxima at 2 mM SO_3^{2-} but 0.5 mM SeO_3^{2-} or TeO_3^{2-} (Supplementary Fig. 2b). The distinct behaviors of SO_3^{2-}, SeO_3^{2-} and TeO_3^{2-} in this reaction could be explained by the discrepancies in the physical properties of S, Se and Te with respect to their sizes, acidities, and bond strengths with a specific element. Regardless, at the optimum concentration, SeO_3^{2-} or TeO_3^{2-} supported cofactor maturation at a level comparable with that achieved by SO_3^{2-} (Fig. 1a). This observation points to the suitability of these compounds as 'labeled' sources of the '9th sulfur'.

Having established the ability of SeO_3^{2-} or TeO_3^{2-} in supporting cofactor maturation, we then conducted continuous wave (CW) EPR analyses to monitor cluster transformation on *Ma*NifB. Consistent with the conversion of two 4Fe clusters (K-cluster) into an 8Fe core (L*-cluster) prior to the incorporation of the '9th sulfur', the SAM-treated *Ma*NifB (designated *Ma*NifB-L*) displayed a distinct change in the line-shape of its $S = 1/2$ signal (Fig. 1b, *blue*) from that of the untreated *Ma*NifB (designated *Ma*NifB-K) (Fig. 1b, *black*) in the dithionite-reduced state. Moreover, in the IDS-oxidized state, an L-cluster-specific signal appeared at $g = 1.94$ in the spectrum of *Ma*NifB-L* (Fig. 1c, *blue*); in comparison, this signal was absent from the spectrum of *Ma*NifB-K (Fig. 1c, *black*). Incubation of *Ma*NifB with SAM and SO_3^{2-}, SeO_3^{2-} or TeO_3^{2-} (designated *Ma*NifB-L, *Ma*NifB-L^{Se} or *Ma*NifB-L^{Te}) resulted in the same line-shape change of the respective $S = 1/2$ signal (Fig. 1b, *green*, *red*, *brown*) as that of *Ma*NifB-L* (Fig. 1b, *blue*) in the dithionite-reduced state, as well as the same $g = 1.94$ signal (Fig. 1c, *green*, *red*, *brown*) as *Ma*NifB-L* (Fig. 1b, *blue*) in the IDS-oxidized state. This observation suggests little to no impact of the insertion of the '9th sulfur' or heavy chalcogenide congeners on the electronic properties of the 8Fe core (*i.e.*, the L*-cluster) despite the observed cofactor maturation activity of the cluster species upon S-, Se- or Te-insertion that clearly distinguishes it from the inactive L*-cluster (Fig. 1a).

The cluster transformation on *Ma*NifB was further examined by three-pulse electron spin echo envelope modulation (3P-ESEEM). Consistent with the presence of a nitrogen ligand for the K1 module of the K-cluster, *Ma*NifB-K demonstrated deep modulations in the time domain of the ESEEM spectrum (Fig. 2a, *black*) and the corresponding intensity between 0–6 MHz in the FFT (Fig. 2b, *black*).[12,17,18] Upon incubation of *Ma*NifB-K with SAM in the absence or presence of SO_3^{2-}, however, the resulting *Ma*NifB-L* (Fig. 2a, b, *blue*) or *Ma*NifB-L (Fig. 2a, b, *green*) no longer displayed the deep modulations to the echo intensity, suggesting a loss of nitrogen coupling upon conversion of the K-cluster to an L*- or L-cluster.[12] The same loss of nitrogen coupling was observed following treatment of *Ma*NifB-K with SAM in the presence of SeO_3^{2-} or TeO_3^{2-} (Fig. 2a, b, *red*, *brown*). The nearly indistinguishable behaviors of the heavy chalcogenide congeners from that of SO_3^{2-} in ESEEM (Fig. 2) and CW EPR (Fig. 1b) experiments, along with the their exchangeability with SO_3^{2-} as the source of the '9th sulfur' in activity assays (Fig. 1a), establish the utility of SeO_3^{2-} and TeO_3^{2-} as suitable spectroscopic probes to trace the incorporation of the '9th sulfur' into the cofactor core.

In pursuit of this line of work, we first performed Fe K-edge XAS/EXAFS analyses of *Ma*NifB-L^{Se} and *Ma*NifB-L^{Te} to assess the overall structure of the Se- and Te-substituted L-clusters. A comparison of the smoothed second derivatives of the pre-edge data in the

XANES regions revealed the structural similarity of the cluster species carried on *Ma*NifB-L^{Se} and *Ma*NifB-L^{Te} to those carried on *Ma*NifB-L* and *Ma*NifB-L (Fig. 3a). As described in our earlier report,[12] the pre-edge spectrum of *Ma*NifB-K consists of a single broad peak centered at ~7112.6 eV (Fig. 3a, *black*), which is typical of the K-cluster (*i.e.*, paired [Fe_4S_4] clusters) with tetrahedral Fe site geometries.[12,19] In comparison, the pre-edge spectra of *Ma*NifB-L* (Fig. 3a, *blue*) and *Ma*NifB-L (Fig. 3a, *green*) have one peak at ~7112.6 eV and a second peak emerging at ~7114.5 eV,[12] which reflects the unusual geometry of the L*- or L-cluster (*i.e.*, the 8Fe core) that is intermediate between tetrahedral and trigonal pyramidal.[12,20] The same double-peak feature is also present in the second derivative of the pre-edge spectra of *Ma*NifB-L^{Se} and *Ma*NifB-L^{Te} (Fig. 3a, *red*, *brown*), suggesting an overall structural similarity of these cluster species to the L*- and L-cluster. Consistent with the similarity of the pre-edge data, the Fe K-edge data for *Ma*NifB-L, *Ma*NifB-L^{Se} and *Ma*NifB-L^{Te} all have similar fits of the EXAFS data, featuring (*i*) Fe–S scatterers at 2.23–2.25 Å, which correspond to the Fourier Transform (FT) features at R+Δ ~1.7 Å; (*ii*) Fe---Fe scatterers at ~2.6 Å from the cubane-like ends of the cluster, which correspond to the FT feature at R+Δ ~2.4 Å; and (*iii*) a long-range Fe---Fe scatterer at ~3.70 Å from the Fe centers across the carbide core, which corresponds to the FT peak at R+Δ ~3 Å (Fig. 3b, c; Supplementary Tables 1–3). Taken together, these observations suggest an overall structural conservation among these cluster species.

With the structural homology of the Fe/S core of the Se- and Te-incorporated L-cluster established, we then explored the transformation of SO_3^{2-} into the '9th sulfur' through Se and Te K-edge XAS/EXAFS analyses. The Se K-edge EXAFS data is best fit with two Se–Fe scatterers at 2.38 Å (Fig. 4a, b, *upper*; Supplementary Tables 4 and 5), suggesting reduction of SeO_3^{2-} upon its incorporation into the L-cluster that results in Se–Fe bond distances observed in synthetic [Fe_4Se_4] clusters.[21,22] The reduction of SeO_3^{2-} is further supported by an apparent change in the rising edge of the normalized fluorescence spectrum of Se species (Fig. 4c, *upper*), as well as the notable absence of a sharp, intense FT feature below R+Δ ~1.5 Å that would have originated from short oxido (S=O) bonds (Fig. 4a, *upper*). While the possible presence of SeO and SeO_2 species cannot be ruled out, inclusion of O scatterers does not improve the fits in a meaningful manner, and the number of S–O scatterers that can be fit is relatively small (N<1). This observation, along with the fact that a substantial amount of Se–Fe scatterers with Se–Fe-type bonds of [Fe_4Se_4] clusters is required for the fit, suggests that a major portion of SeO_3^{2-} has been fully reduced to Se^{2-}. Paired with the Fe K-edge data, the Se K-edge data points to a possible route of SeO_3^{2-} incorporation as Se^{2-} into the belt position of the L-cluster.

Like SeO_3^{2-}, TeO_3^{2-} also undergoes reduction upon its incorporation into the L-cluster, as indicated by a clear change in the rising edge of the normalized fluorescence spectrum of Te species (Fig. 4c, *lower*) and the absence of the characteristic FT feature of short oxido (Te=O) bonds (Fig. 4a, *lower*). Unlike the Se K-edge data, however, the Te K-edge data is best fit with (*i*) one Te–Fe interaction at 2.55 Å, which is consistent with Te–Fe bonds found in the crystal structures of FeTe complexes, including [Fe_4Te_4] clusters;[23,24] and (*ii*) two longer Te---Fe distances at 2.79 Å, which are too long to be formal bonds given the crystallographically determined range of Fe–Te bonds between 2.5 and 2.7 Å (Fig. 4a, b, *lower*; Supplementary Tables 4 and 6). Inclusion of O scatterers does not yield a substantive

improvement on the goodness of fit parameters, although the small FT peaks between R+Δ ~ 1–2 Å (Fig. 4a, *lower*) can be fit with Te–O distances at ~1.9 and 2.1 Å (Supplementary Table 6). This observation implies that a small portion of the Te species has an oxygen ligand(s), although the majority of the Te species is likely free of oxygen, as indicated by the necessity to include a large number of Te–Fe distances typically found in the FeTe complexes and a relatively small number of Te–O distances for the fit.

Based on the Fe, Se and Te K-edge data, it can be proposed that SeO_3^{2-} is mostly inserted as a μ_2-belt Se^{2-} that is bridged symmetrically between a pair of cluster Fe atoms of the L^{Se}-cluster (in *Ma*NifB-L^{Se}); whereas TeO_3^{2-} is mainly inserted as a belt Te^{2-}-like species that forms a bond with one of the cluster Fe atoms of the L^{Te}-cluster (in *Ma*NifB-L^{Te}) and additionally interacts with two other Fe atoms at a longer distance than a formal bond (Fig. 4d). Together, these observations indicate that SO_3^{2-} is incorporated as S^{2-} in the belt region of the L-cluster. Consistent with this argument, incubation of the SAM-treated *Ma*NifB with $^{34}SO_3^{2-}$ in the presence of Eu^{II}-EGTA, followed by acid quenching, resulted in the release of the acid labile, cluster-bound $^{34}S^{2-}$ as $H_2{}^{34}S$ (Supplementary Fig. 2c). The possible presence of a small portion of XO or XO_2 species (X=Se, Te), particularly in the case of Te, may originate from an incomplete reduction of these 'unnatural', heavy chalcogenide congeners *en route* to fully reduced X^{2-} species. Moreover, the configurations of both the fully reduced species (X^{2-}) and the partially reduced intermediates (XO or XO_2) point to the possibility of *in situ* reduction of SO_3^{2-} to S^{2-} at the 'vacant' belt site during the insertion of the '9th sulfur'.

To further explore the insertion mechanism of the '9th sulfur', we performed DFT calculations of the energetics of the coordination of XO_3^{2-} species (X= S, Se, or Te) to the '9th sulfur'-deficient L*-cluster (*see* Supplementary Methods for computational details). For the initial coordination step, we considered two possible binding scenarios for XO_3^{2-}: one scenario involves coordination of one cluster Fe atom by the X atom, and another cluster Fe atom by one O atom of the XO_3^{2-} ligand (Fig. 5a, *the 'one O route'*); whereas the other scenario involves coordination of two O atoms of the XO_3^{2-} ligand by two cluster Fe atoms, each O atom ligated by one cluster Fe atom (Fig. 5b, *the 'two O route'*). As illustrated by the calculated reaction energies, the coordination and the subsequent, complete reduction of XO_3^{2-} to X^{2-} at the 'vacant' belt site of the L*-cluster are energetically feasible in both scenarios, independent of the nature of the X atom (Fig. 5a, b). However, when the cumulative reaction energy is plotted *versus* the reaction step, it would appear that the S species favors the 'one O route', while the Se and Te compounds favor the 'two O route', especially when the energy of the first reduction step is considered (Fig. 5c). Given the pK_a values of H_2XO_3,[25–27] it is plausible that the terminal O atoms of SeO_3^{2-} and TeO_3^{2-} have higher basicity and stronger tendency to donate electrons to metals than the terminal O atoms of SO_3^{2-}. Such a discrepancy in electron donating ability, along with the size difference among X atoms (S<Se<Te), could contribute to the preference of SO_3^{2-} for the 'one O route' and the preference of SeO_3^{2-} and TeO_3^{2-} for the 'two O route' at the beginning of the reaction. But more importantly, the overall energetic feasibility of this type of reaction suggests a cluster-facilitated, *in situ* reduction of the XO_3^{2-} species via dissociation of water molecules.

The observation that the '9th sulfur' position needs to be occupied by an XO_3^{2-}-derived species in order to achieve cofactor maturation activity led to the question of the role played by the '9th sulfur' in this process. To address this question, we incubated a non-tagged form of NifB with a His-tagged form of apo-NifEN in the presence of SAM with or without XO_3^{2-}, separated NifEN from NifB after incubation, matured the L-cluster species on NifEN, and subsequently examined the ability of NifEN to donate M-clusters to apo-NifDK. Interestingly, NifEN incubated with NifB in the presence of XO_3^{2-} was capable of donating M-clusters for the reconstitution of apo-NifDK; whereas NifEN incubated with NifB in the absence of XO_3^{2-} was inactive in this reaction (Fig. 6a). CW EPR analysis further revealed the presence of the L-cluster-specific, $g = 1.96$ signal in the spectrum of NifEN prepared with XO_3^{2-}, and the absence of this signal from the spectrum of NifEN prepared without XO_3^{2-} (Fig. 6b). The fact that the L*-cluster with a 'vacant' belt site cannot be transferred from NifB to NifEN suggests a crucial role of the '9th sulfur' in stabilizing the cluster for inter-protein cluster transfer. Moreover, the comparable substrate-reducing activities of the NifDK proteins reconstituted with the S-, Se- and Te-containing M-clusters (Fig. 6a; *also see* Fig. 1a) could be explained by a plausible cluster rotation mechanism that involves substrate binding and product release via dynamic displacement and replacement of belt sulfurs during catalysis (Supplementary Fig. 3).[28] In this scenario, the displacement of S, Se or Te is eventually followed by a 'refill' with S, which renders the S-, Se- and Te-containing M-clusters indistinguishable from one another in their catalytic capabilities.

Conclusion

Using SeO_3^{2-} and TeO_3^{2-} as a labeled SO_3^{2-} source, we have successfully traced the incorporation of SO_3^{2-} as the '9th S^{2-}' into the belt region of the L-cluster, an $[Fe_8S_9C]$ precursor of the nitrogenase cofactor. Our results have provided strong support for the appearance of the L*-cluster, an $[Fe_8S_8C]$ precursor that represents the core geometry of the cofactor but lacks the '9th sulfur' in the belt region, prior to the $[Fe_8S_9C]$ L-cluster along the cofactor biosynthetic pathway; moreover, these results have led to the proposal of a plausible mechanism of *in situ* reduction of SO_3^{2-} to S^{2-} at the 'vacant' belt site, a process initiated via coordination of the S/O atoms of SO_3^{2-} to a pair of Fe atoms across the belt. The insertion of the '9th belt sulfur' during cofactor biosynthesis loosely mirrors the proposed 'refilling' of the belt-sulfur-displaced sites during nitrogenase catalysis (Supplementary Fig. 3),[28] both of which reflect the labile nature of the belt region of the cofactor[29,30] that is crucial for the assembly and mechanism of nitrogenase. In the case of the former, insertion of the '9th sulfur' in the belt region stabilizes the cofactor precursor, allowing it to be transferred as an intact unit to the next receptor protein; whereas in the case of the latter, the displacement and refilling of belt sulfur(s) may facilitate release of the products and continuation of catalysis. In both cases, the spectroscopic evidence reported herein seems to point to a weakly ligated atom (S, Se, or Te) that may act more like a −2 counter charge than a coordinating ligand in the belt region of the L- or M-cluster, which could account for the insensitivity of the spectral data to the identity and coordination of this belt atom. Importantly, the feasibility to use 'labeled' SO_3^{2-} as the source of the '9th sulfur', as established in this work, could prove instrumental for labeling the catalytically

important belt region of the nitrogenase cofactor, which will in turn facilitate mechanistic investigations of nitrogenase-catalyzed reactions.

Supplementary Material

Refer to Web version on PubMed Central for supplementary material.

Acknowledgements

This work was supported by NIH-NIGMS grants GM67626 (to M.W.R. and Y.H.), GM141046 (to Y.H. and M.W.R.), R35 GM126961 (to R.D.B.), GM110501 (to J.Y.), and GM126289 (to J.K.). Y.O. was supported by Grant-in-Aids for Scientific Research (MEXT Japan) (numbers 19H02733 and 20K21207), International Collaborative Research Program of ICR, Kyoto University, Takeda Science Foundation, and Tatematsu Foundation. K.T. recieved support from the Kyoto University Research Fund for Young Scientist (Start-Up). XAS data were collected at Beamlines 7–3 and 9–3 at the Stanford Synchrotron Radiation Lightsource, SLAC National Accelerator Laboratory. SLAC is supported by the U.S. Department of Energy, Office of Science, Office of Basic Energy Sciences under Contract No. DE-AC02–76SF00515. The SSRL Structural Molecular Biology Program is supported by the DOE Office of Biological and Environmental Research, and by the National Institutes of Health, National Institute of General Medical Sciences (including P30GM133894).

Data Availability

The authors declare that all data supporting the findings of this study are available within the article, the supplementary information and the source files published alongside the article.

References

1. Burgess BK & Lowe DJ Mechanism of molybdenum nitrogenase. Chem. Rev. 96, 2983–3012 (1996). [PubMed: 11848849]
2. Buscagan TM & Rees DC Rethinking the nitrogenase mechanism: activating the active site. Joule 3, 2662–2678 (2019). [PubMed: 32864580]
3. Rutledge HL & Tezcan FA Electron transfer in nitrogenase. Chem. Rev. 120, 5158–5193 (2020). [PubMed: 31999100]
4. Jasniewski AJ, Lee CC, Ribbe MW & Hu Y Reactivity, mechanism, and assembly of the alternative nitrogenases. Chem. Rev. 120, 5107–5157 (2020). [PubMed: 32129988]
5. Spatzal T, Aksoyoglu M, Zhang L, Andrade SLA, Schleicher E, Weber S, Rees DC & Einsle O Evidence for interstitial carbon in nitrogenase FeMo cofactor. Science 334, 940 (2011). [PubMed: 22096190]
6. Wiig JA, Hu Y, Lee CC & Ribbe MW Radical SAM-dependent carbon insertion into the nitrogenase M-cluster. Science 337, 1672–1675 (2012). [PubMed: 23019652]
7. Lee SC, Lo W & Holm RH Developments in the biomimetic chemistry of cubane-type and higher nuclearity iron-sulfur clusters. Chem. Rev. 114, 3579–3600 (2014). [PubMed: 24410527]
8. Ohki Y & Tatsumi K New synthetic routes to metal-sulfur clusters relevant to the nitrogenase metallo-clusters. Z. Anorg. Allg. Chem. 639, 1340–1349 (2013).
9. Ribbe MW, Hu Y, Hodgson KO & Hedman B Biosynthesis of nitrogenase metalloclusters. Chem. Rev. 114, 4063–4080 (2014). [PubMed: 24328215]
10. Hu Y & Ribbe MW Biosynthesis of the Metalloclusters of Nitrogenases. Annu. Rev. Biochem. 85, 455–483 (2016). [PubMed: 26844394]
11. Tanifuji K, Lee CC, Sickerman NS, Tatsumi K, Ohki Y, Hu Y & Ribbe MW Tracing the ‘ninth sulfur’ of the nitrogenase cofactor via a semi-synthetic approach. Nat. Chem. 10, 568–572 (2018). [PubMed: 29662207]
12. Jasniewski AJ, Wilcoxen J, Tanifuji K, Hedman B, Hodgson KO, Britt RD, Hu Y & Ribbe MW Spectroscopic characterization of an eight-iron nitrogenase cofactor precursor that lacks the “9th sulfur”. Angew. Chem. Int. Ed. Engl. 58, 14703–14707 (2019). [PubMed: 31411369]

13. Hu Y, Corbett MC, Fay AW, Webber JA, Hodgson KO, Hedman B & Ribbe MW FeMo cofactor maturation on NifEN. Proc. Natl. Acad. Sci. U. S. A. 103, 17119–17124 (2006). [PubMed: 17050696]
14. Hu Y, Corbett MC, Fay AW, Webber JA, Hodgson KO, Hedman B & Ribbe MW Nitrogenase Fe protein: A molybdate/homocitrate insertase. Proc. Natl. Acad. Sci. U. S. A. 103, 17125–17130 (2006). [PubMed: 17062756]
15. Hu Y & Ribbe MW Maturation of nitrogenase cofactor-the role of a class E radical SAM methyltransferase NifB. Curr. Opin. Chem. Biol. 31, 188–194 (2016). [PubMed: 26969410]
16. Kang W, Rettberg L, Stiebritz M, Jasniewski A, Tanifuji K, Lee CC, Ribbe MW & Hu Y Crystallographic analysis of NifB with a full complement of clusters: Structural insights into the radical SAM-dependent carbide insertion during nitrogenase cofactor assembly. Angew. Chem. Int. Ed. Engl. (2020) 10 9. doi: 10.1002/anie.202011367. Online ahead of print.
17. Rettberg LA, Wilcoxen J, Jasniewski AJ, Lee CC, Tanifuji K, Hu Y, Britt RD & Ribbe MW Identity and function of an essential nitrogen ligand of the nitrogenase cofactor biosynthesis protein NifB. Nat. Commun. 11, 1757 (2020). [PubMed: 32273505]
18. Rettberg LA, Wilcoxen J, Lee CC, Stiebritz MT, Tanifuji K, Britt RD & Hu Y Probing the coordination and function of Fe_4S_4 modules in nitrogenase assembly protein NifB. Nat. Commun. 9, 2824 (2018). [PubMed: 30026506]
19. Musgrave KB, Angove HC, Burgess BK, Hedman B, & Hodgson KO All-ferrous titanium(iii) citrate reduced Fe protein of nitrogenase: an XAS study of electronic and metrical structure. J. Am. Chem. Soc. 120, 5325–5326 (1998).
20. Einsle O, Tezcan FA, Andrade SLA, Schmid B, Yoshida M, Howard JB, Rees DC Nitrogenase MoFe-protein at 1.16 A resolution: a central ligand in the FeMo-cofactor. Science 297, 1696–1700 (2002). [PubMed: 12215645]
21. Ciurli S, Yu SB, Holm RH, Srivastava KKP & Munck E Synthetic nickel-iron $NiFe_3Q_4$ cubane-type clusters (S = 3/2) by reductive rearrangement of linear $[Fe_3Q_4(SEt)_4]^{3-}$ (Q = sulfur, selenium). J. Am. Chem. Soc. 112, 8169–8171 (1990).
22. Bobrik MA, Laskowski EJ, Johnson RW, Gillum WO, Berg JM, Hodgson KO & Holm RH Selenium substitution in $[Fe_4S_4(SR)_4]^{2-}$: synthesis and comparative properties of $[Fe_4X_4(YC_6H_5)_4]^{2-}$ (X, Y = sulfur, selenium) and the structure of $[(CH_3)_4N]_2[Fe_4Se_4(SC_6H_5)_4]$. Inorg. Chem. 17, 1402–1410 (1978).
23. Barbaro P, Bencini A, Bertini I, Briganti F & Midollini S The tetranuclear trianion $[Fe_4Te_4(SC_6H_5)_4]^{3-}$: crystal and molecular structure and magnetic properties. J. Am. Chem. Soc. 112, 7238–7246 (1990).
24. Simon W, Wilk A, Krebs B & Henkel G $[Fe_4Te_4(TePh)_4]^{3-}$, the first telluride-tellurolate complex. Angew. Chem. Int. Ed. Engl. 26, 1009–1010 (1987).
25. Zimmermann MD & Tossell JA Acidities of arsenic (III) and arsenic (V) thio- and oxyacids in aqueous solution using the CBS-QB3/CPCM method. J. Phys. Chem. A 113, 5105–5111 (2009). [PubMed: 19351160]
26. URL: https://pubchem.ncbi.nlm.nih.gov/compound/1091
27. URL: https://pubchem.ncbi.nlm.nih.gov/compound/24936
28. Kang W, Lee CC, Jasniewski AJ, Ribbe MW & Hu Y Structural evidence for a dynamic metallocofactor during N_2 reduction by Mo-nitrogenase. Science 368, 1381–1385 (2020). [PubMed: 32554596]
29. Spatzal T, Perez KA, Howard JB & Rees DC Catalysis-dependent selenium incorporation and migration in the nitrogenase active site iron-molybdenum cofactor. Elife 4, e11620 (2015). [PubMed: 26673079]
30. Spatzal T, Perez KA, Einsle O, Howard JB & Rees DC Ligand binding to the FeMo-cofactor: structures of CO-bound and reactivated nitrogenase. Science 345, 1620–1623 (2014). [PubMed: 25258081]

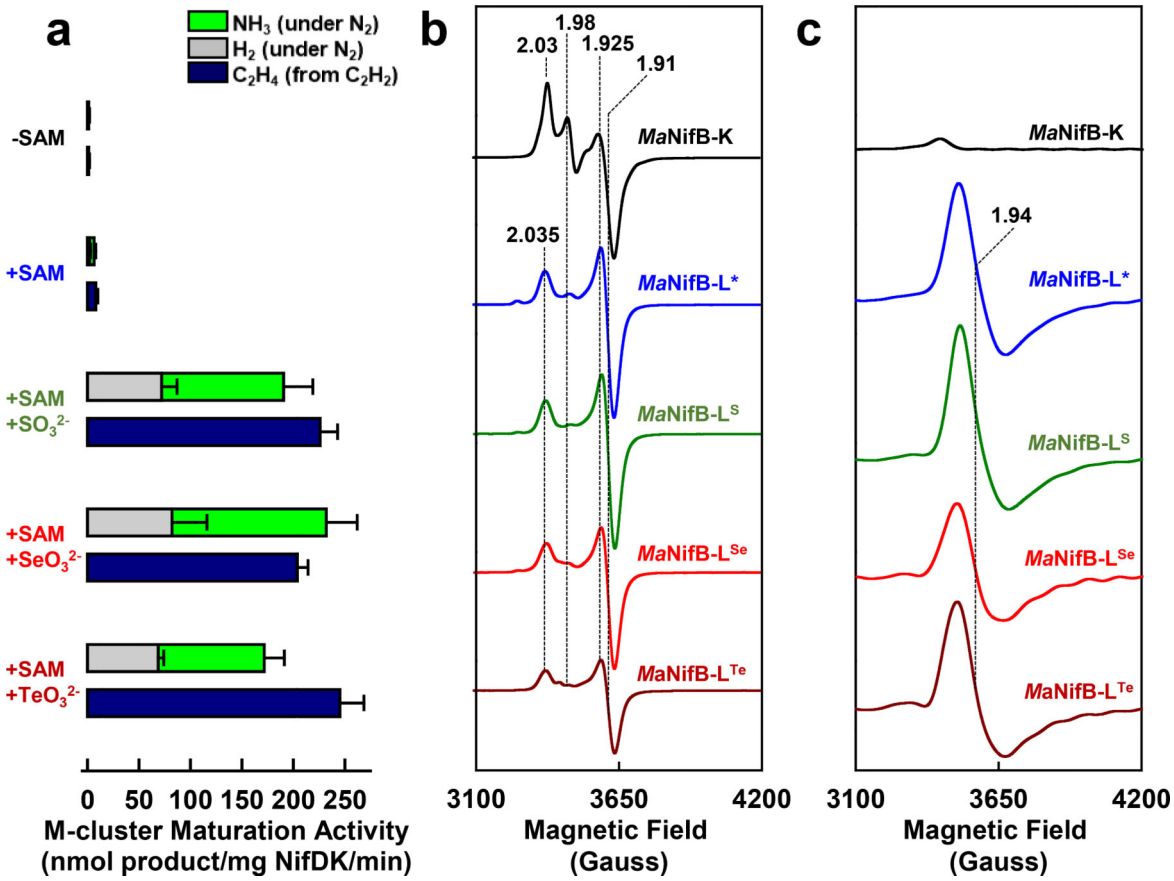

Fig. 1. Incorporation of S, Se and Te into the L*-cluster.

(**a**) M-cluster maturation activity of *Ma*NifB (carrying the K-cluster) without treatment with any additive or upon incubation with SAM alone, SAM plus SO_3^{2-}, SAM plus SeO_3^{2-}, and SAM plus TeO_3^{2-}. Eu^{II}-EGTA, a sulfur-free reductant, was used in these assays. Activity data were obtained from three independent experiments (n=6) and presented as mean±s.d. Activities were normalized based on the L-cluster contents. (**b**, **c**) EPR spectra of (**b**) dithionite-reduced and (**c**) IDS-oxidized *Ma*NifB (carrying the K-cluster) without treatment with any additive (*Ma*NifB-K; *black*) or upon treatment with SAM (designated *Ma*NifB-L*; *blue*), SAM plus SO_3^{2-} (designated *Ma*NifB-L^S; *green*), SAM plus SeO_3^{2-} (designated *Ma*NifB-L^{Se}; *red*), and SAM plus TeO_3^{2-} (designated *Ma*NifB-L^{Te}; *brown*). The spectra were recorded as described in *Methods*. Shown are the representative spectra of three independent experiments (n=3). The *g* values are indicated.

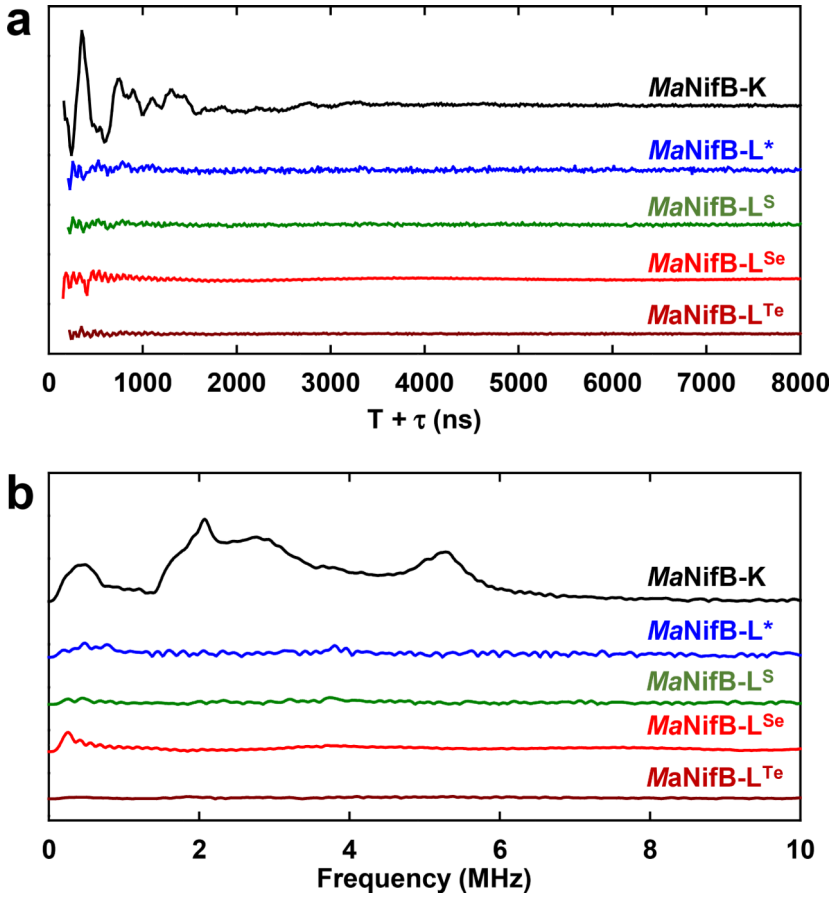

Fig. 2. Three-pulse ESEEM spectra of various *Ma*NifB proteins.

(**a**) Time domain and (**b**) fast Fourier transformed (FFT) spectra of *Ma*NifB-K (*black*), *Ma*NifB-L* (*blue*), *Ma*NifB-L^S (*green*), *Ma*NifB-L^{Se} (*red*), and *Ma*NifB-L^{Te} (*brown*). The large modulations observed in the time trace (a) and the corresponding FFT peaks of *Ma*NifB-K between 0–6 MHz (b) are characteristic of the hyperfine coupling of a nitrogen coordinating the K1 cluster. These modulations from the ligating nitrogen are lost upon formation of the L*-, L^S-, L^{Se}- and L^{Te}-clusters. Experimental conditions: $\pi/2$ width=12 ns, τ=128 ns, T increments=16 ns, frequency=9.816 GHz, temperature=10 K. Shown are the representative spectra from two independent experiments (n=2).

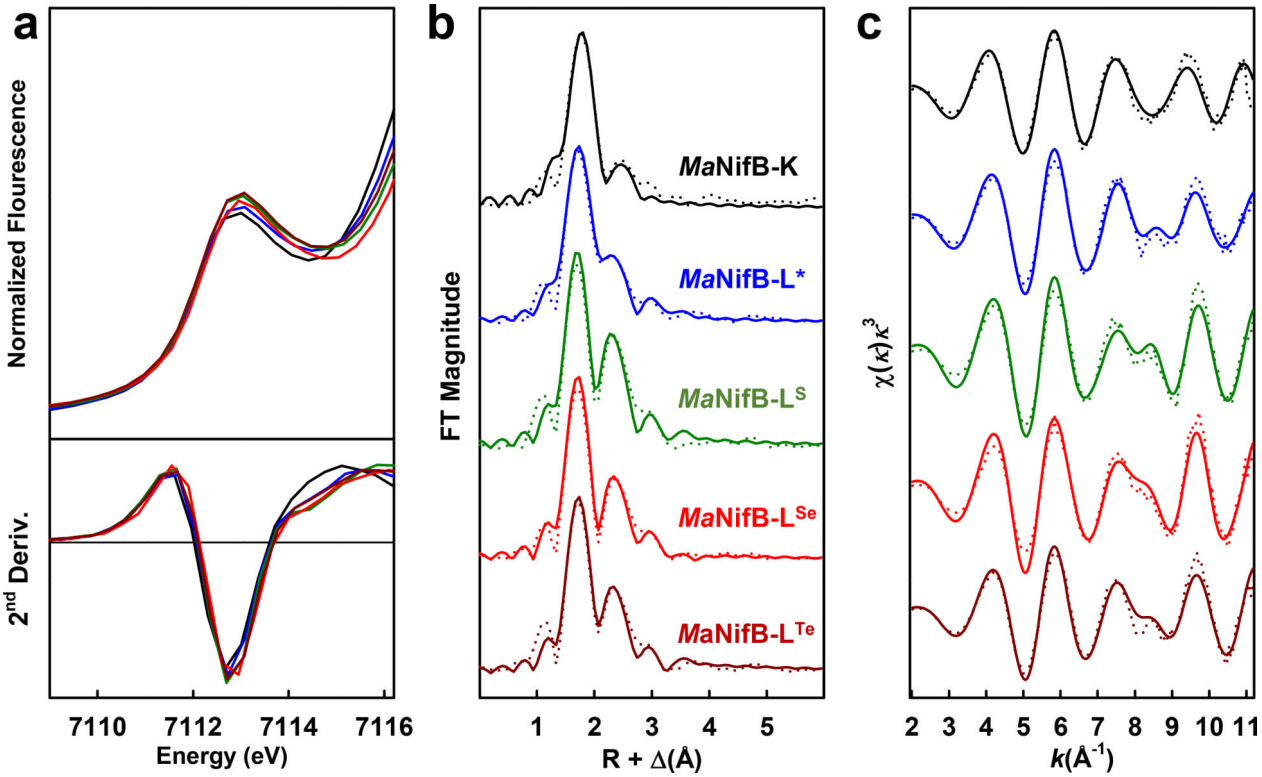

Fig. 3. Fe K-edge XAS analysis of of various *Ma*NifB proteins.

(**a**) Pre-edge regions of the normalized fluorescence spectra (*upper*) and smoothed second derivatives of the pre-edge regions (*lower*), (**b**) Fourier transforms of the EXAFS data (*dotted*) and the best fits of data (*solid*), and (**c**) k^3-weighted EXAFS data (*dotted*) and the best fits of data (*solid*) of *Ma*NifB-K (*black*), *Ma*NifB-L* (*blue*), *Ma*NifB-L^S (*green*), *Ma*NifB-L^{Se} (*red*), and *Ma*NifB-L^{Te} (*brown*). See Supplementary Tables 1–3 for detailed EXAFS fits.

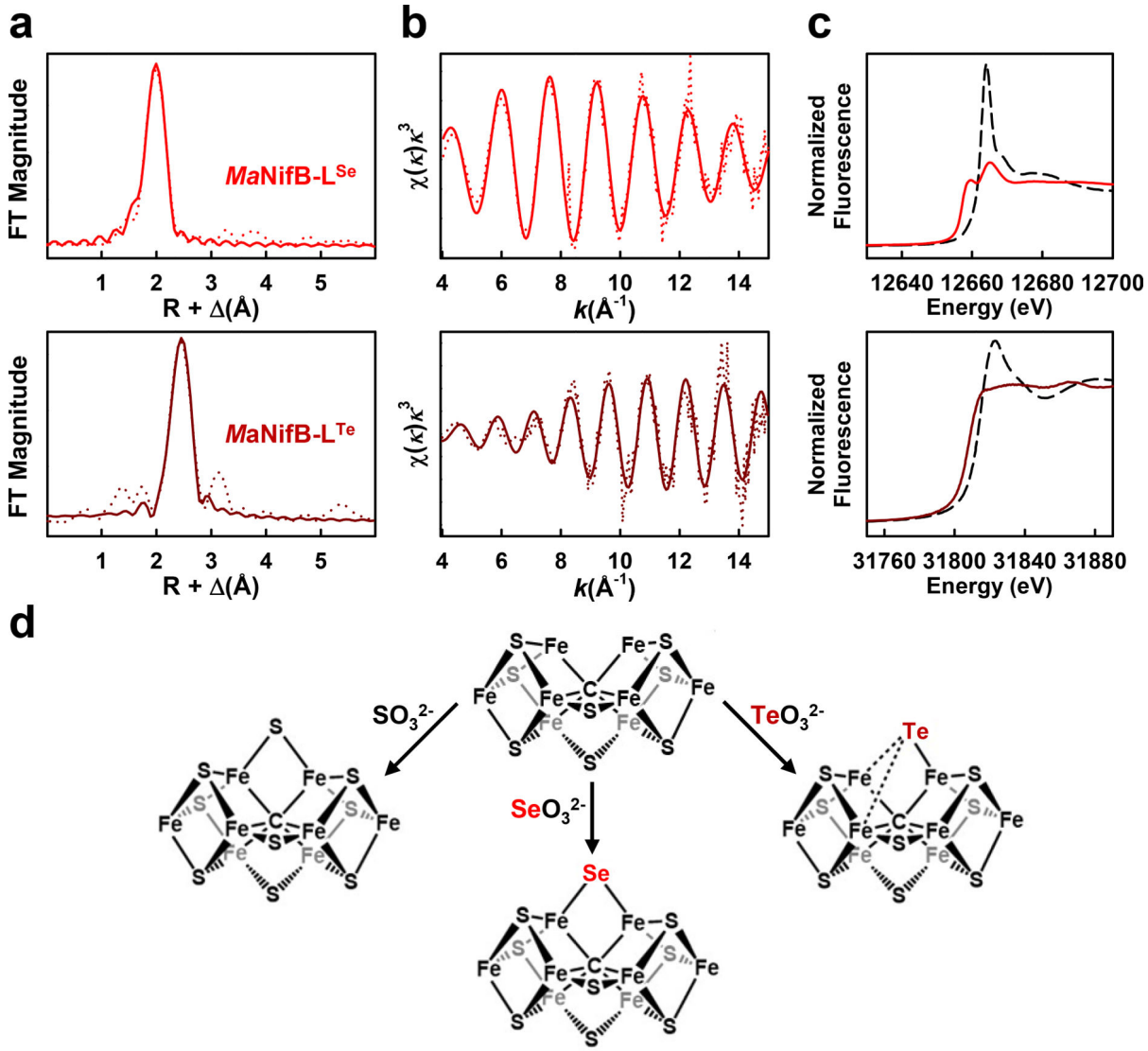

Figure 4. Se and Te K-edge EXAFS analyses of of various *Ma*NifB proteins.

(**a**) Fourier transforms of Se (*upper*) and Te (*lower*) K-edge EXAFS data (*dotted*) and the best fits of data (*solid*), (**b**) k^3-weighted EXAFS data (*dotted*) and the best fits of data (*solid*) of *Ma*NifB-L^{Se} (*upper*) and *Ma*NifB-L^{Te} (*lower*) (see Supplementary Tables 4–6 for detailed EXAFS fits), (**c**) spectra of the rising edges of the Se (*upper*) and Te (*lower*) normalized K-edge fluorescence spectra for *Ma*NifB-L^{X} (*solid*) and the corresponding Na_2XO_3 (X=Se, Te) references (*dashed*), and (**d**) schemes of the reactions the L*-cluster could undergo within the *Ma*NifB protein scaffold based on EXAFS data analysis.

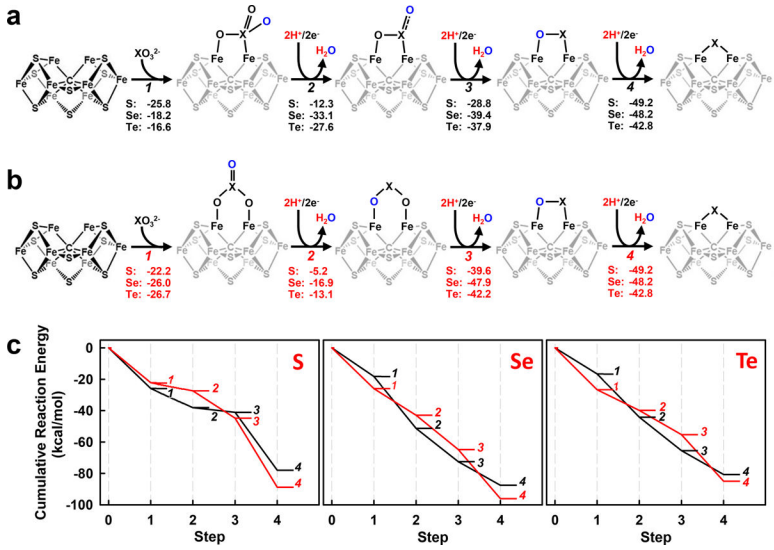

Fig. 5. Coordination and reduction of XO_3^{2-} (X = S, Se, Te) at the free binding site of an under-coordinated L*-cluster.

Reaction energies of the (**a**) first and (**b**) second coordination scenario, obtained from DFT calculations (TPSS/def2-TZVP, COSMO e=20, DFT-D3) on L-cluster models with the assumption that coupled e^-/H^+ transfer occurs after the initial coordination step. The energies (kcal/mol) for S, Se, and Te incorporation are indicated in the schemes. (**c**) Cumulative reaction energies of S (*left*), Se (*middle*) and Te (*right*) incorporation from the corresponding XO_3^{2-} (X=S, Se, Te) species for the first (*black*) and second (*red*) coordination scenario.

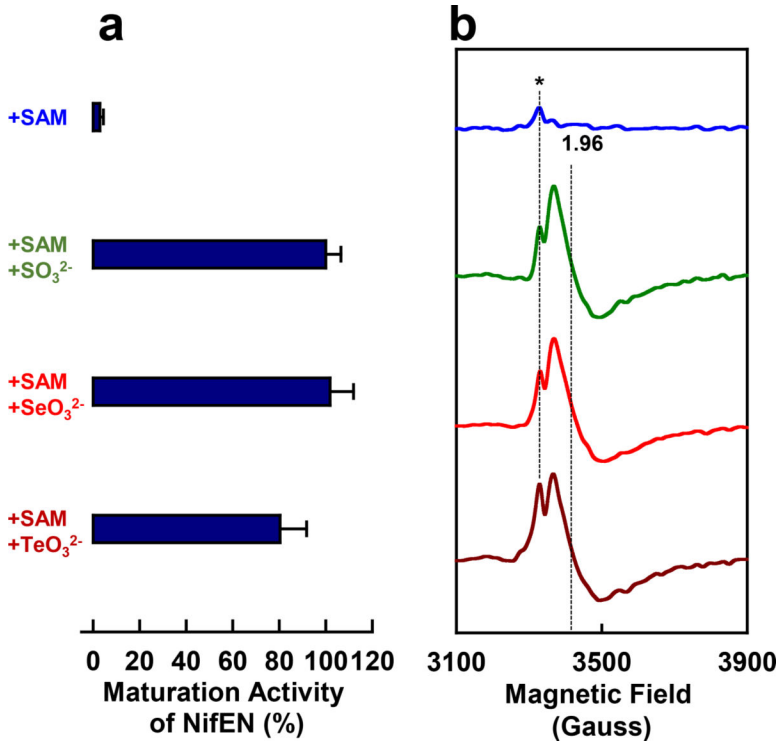

Fig. 6. The role of the '9th sulfur' in cluster transfer from NifB to NifEN.

(**a**) M-cluster maturation activity and (**b**) EPR spectra of the IDS-oxidized NifEN that was re-purified after incubation with NifB-L* (*blue*), NifB-L^S (*green*), NifB-L^{Se} (*red*) and NifB-L^{Te} (*brown*). NifB-L*, NifB-L^S, NifB-L^{Se} and NifB-L^{Te} were generated upon incubation of NifB-K with SAM in the absence and presence of the respective XO_3^{2-} (X=S, Se, Te) species as indicated in the figure. The maximum maturation activity, 71±5 nmol C_2H_4/mg NifDK/min, was set as 100%, and the percentage maturation activity was calculated accordingly (a). Activity data were obtained from three independent experiments (n=6) and presented as mean±s.d. The EPR spectra were recorded as described in *Methods*, and the *g* value of the L-cluster-specific signal is indicated (b). Shown are the representative spectra from three independent experiments (n=3). An impurity occasionally observed at g = 2.01 in the spectra of IDS-oxidized samples is indicated by *.